

# Substrate Role in Polaron Formation on Single-layer Transition Metal Dihalides

Affan Safeer,<sup>1,\*</sup> Oktay Gülerüz,<sup>1</sup> Guangyao Miao,<sup>1</sup>  
Wouter Jolie,<sup>1</sup> Thomas Michely,<sup>1</sup> and Jeison Fischer<sup>1</sup>

<sup>1</sup>*II. Physikalisches Institut, Universität zu Köln,  
Zùlpicher Straße 77, 50937 Köln, Germany*

## Abstract

Single-layer transition metal dihalides grown on conducting substrates were shown to host stable polarons. Here, we investigate polarons in insulating single-layer  $\text{MnBr}_2$  grown by molecular beam epitaxy on three different substrates, namely graphene on Ir(110), graphene on Ir(111), and Au(111). The number densities and species of polarons observed vary strongly as a function of the substrate. For  $\text{MnBr}_2$  grown on Ir(110) the largest number of polaron species is observed, namely four, of which three show clear similarities with the species observed for  $\text{CoCl}_2$  on graphite. Polarons in single-layer  $\text{MnBr}_2$  are observed up to 300 K. They can be created, converted, and moved by the STM tip when a tunneling current flows at a proper bias voltage. For graphene on Ir(110) as a substrate, mobile polarons in  $\text{MnBr}_2$  are guided through the periodic potential imposed from the super-moiré resulting from the interaction of  $\text{MnBr}_2$  with graphene and Ir(110). Our findings indicate that modeling of polarons in such single-layer insulators in contact with a conducting substrate requires to take the substrate explicitly into account.

---

\* [safeer@ph2.uni-koeln.de](mailto:safeer@ph2.uni-koeln.de)

## INTRODUCTION

An excess charge carrier (electron or hole) introduced into a polarizable material can couple to the lattice vibration and distort the surrounding ions, creating a local lattice distortion bound to the carrier. The resulting composite quasiparticle (a charge dressed by lattice distortion) is called a polaron. Depending on the spatial extent of electron-phonon coupling, one commonly distinguishes small or Holstein polarons, where the distortion is confined to one or a few lattice sites, and large or Fröhlich polarons, where both the lattice distortion and charge carrier wave function extend over many unit cells [1]. Polarons can strongly modify charge transport properties by increasing the effective mass or promoting thermal-activated hopping, and can also affect other properties such as chemical reactivity (detail reviewed in ref. 1). Correspondingly, polarons are central to the functional behavior and technological use of many materials, for example, transition metal oxides [2–5], where charge transport is often governed by small polarons and halide perovskites [6, 7], where large polarons are frequently invoked.

Although polarons in solids can be detected with a multitude of methods, the ability of scanning tunneling microscopy (STM) and - spectroscopy (STS) to visualize the charge distribution at a surface has made a substantial impact for the development of the field. Considering the paradigmatic example of small polarons in rutile  $\text{TiO}_2$ , excess charge carriers are introduced into the unoccupied  $3d$  states of Ti atoms next to surface oxygen vacancies created, e.g., by vacuum annealing. Using STM, STS and ab initio calculations the resulting charge distribution was measured [8] and unambiguously identified to be due to small polarons [9]. Since then, local probe experiments have been instrumental in improving our understanding of small polarons [10–16].

Evidently, 2D materials with their reduced screening are also candidates for polaron formation, although no evidence for polarons in 2D materials was published until 2018. A first report on a polaron in a 2D material was of interface polarons between hexagonal boron nitride and graphene, detected by angle-resolved photoemission [17]. Using the same method, polarons were reported in doped  $\text{MoS}_2$  [18], but this interpretation was convincingly questioned [19, 20]. Recently, based on STS and STM, the existence of polarons in doped single-layer  $\text{MoS}_2$  was proposed [21].

A breakthrough occurred and a new paradigm evolved, when two back-to-back studies

demonstrated the creation, annihilation, and manipulation of small polarons by a STM tip in epitaxially grown single-layer  $\text{CoCl}_2$  [22, 23]. These findings were later extended to other members of the family of transition metal dihalides, including  $\text{FeCl}_2$  [22],  $\text{CrI}_2$  [24],  $\text{NiI}_2$  [25], and  $\text{CrBr}_3$  [26]. Complementary ab initio calculations were stimulated by the observed manifold of polarons, their stability, and the ease by which they can be manipulated with the STM tip [22, 23, 26, 27]. In addition to the small polaron interpretation for  $\text{CoCl}_2$ , an alternative scenario of solitons due to charge dipoles has also been proposed [28, 29].

Here, we investigate polarons in single-layer  $\text{MnBr}_2$ , a transition metal dihalide that has not yet been explored from this perspective. Mn has the lowest electronegativity among the transition metals, enhancing ionic interactions with halides and thus ionic polarizability, a key factor for polaron formation [20]. The half-filled  $3d^5$  configuration of Mn diminishes electron hopping, leads to a flat conduction band with d-character [30], a favorable condition for electron localization. Lastly, although electron-phonon coupling in  $\text{MnBr}_2$  has not been investigated, its phonons are soft with maximal energies of the order of 20 meV [30, 31], i.e., there is comparatively little energy involved in deformation of the  $\text{MnBr}_2$  lattice.

Although our results show some similarities with those for polarons in single layers of  $\text{CoCl}_2$  on graphite, we uncover a number of new aspects. The emergence of a polaron species not reported so far, the strong interaction of polarons with a super-moiré resulting from the interaction of  $\text{MnBr}_2$  with its substrate, and an impressive thermal stability of polarons. Most importantly, a hitherto somewhat overlooked strong dependence of the polaron phenomenology on the substrate is identified. This substrate dependence has profound implications for understanding polaron formation.

Single-layer  $\text{MnBr}_2$  has been investigated theoretically using density functional theory (DFT) [30–35]. In the single layer, Mn ions with  $\approx 5\mu_B$  magnetic moments are predicted in most studies to be antiferromagnetically ordered. Not surprising, bulk  $\text{MnBr}_2$  displays below 2.35 K antiferromagnetic ordering [36–39].

In a previous experimental study [40] single-layer  $\text{MnBr}_2$  grown on Gr/Ir(110) displayed the same structure as a layer in the van der Waals bulk material, that is, in a hexagonal  $\text{CdI}_2$ -type lattice in which six  $\text{Br}^-$  ions sandwich the  $\text{Mn}^{2+}$  ions and coordinate them in an edge-sharing arrangement. The experimental lattice constant of 3.90 Å closely matches the bulk lattice parameter of 3.873 Å [41], confirming structural integrity of  $\text{MnBr}_2$  in the single-layer limit. Single-layer  $\text{MnBr}_2$  on Gr/Ir(110) is an insulator with an experimental

band gap of 4.4 eV [40], slightly larger than the DFT predictions of 4.21 eV [31] or 3.95 eV [30] for the freestanding single-layer. Of specific relevance for the present work is the fact that  $\text{MnBr}_2$  on  $\text{Gr}/\text{Ir}(110)$  forms a complex super-moiré arising from the superposition of the  $\text{MnBr}_2/\text{Gr}$ ,  $\text{MnBr}_2/\text{Ir}(110)$ , and  $\text{Gr}/\text{Ir}(110)$  moirés [40].

## RESULTS

### Polaron Phenomenology and interaction with the super-moiré

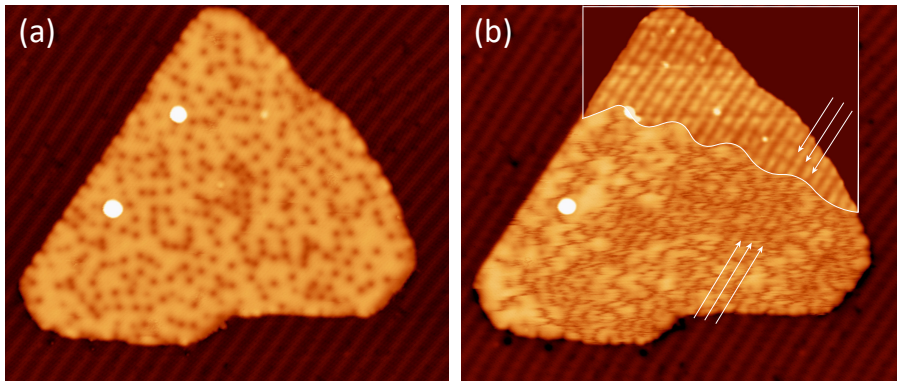


Figure 1. Polaron mobility. (a) Single-layer  $\text{MnBr}_2$  island imaged by STM with  $V_b = 2.5$  V,  $I_t = 20$  pA. At this  $V_b$ , polarons are immobile. (b) Same island as in (a), but  $V_b = 3$  V,  $I_t = 20$  pA. Polarons fluctuate in position under the influence of the STM tip. Inset bounded by white line displays the same island as in (a), but imaged at  $V_b = -1$  V. At this voltage, the  $\text{MnBr}_2/\text{Gr}/\text{Ir}(110)$  super-moiré is visible. STM topographs are taken at 4.2 K. Images sizes: 100 nm  $\times$  85 nm.

Figure 1(a) displays a low-temperature STM topograph of a single-layer  $\text{MnBr}_2$  island acquired at  $V_b = 2.5$  V. A high density of depressions is visible with a diameter of the order of  $\approx 2$  nm at half depth and a maximum apparent depth of  $\approx 2$  Å. Upon increasing  $V_b$  to 3.0 V, most dark spots transform into fuzzy stripe-like features. These dark fuzzy stripe-like features follow the stripes of the  $\text{MnBr}_2/\text{Gr}/\text{Ir}(110)$  super-moiré with a wavelength of  $\lambda_{sm} \approx 2.7$  nm. This becomes obvious through the inset of Figure 1(b), which is taken at  $V_b = -1.0$  V, a voltage where for this magnification only the dominant Fourier component of the super-moiré is visible [40]. Two sets of white arrows emphasize the 2.7 nm periodicity of the super-moiré. In the surrounding of the island the  $\text{Gr}/\text{Ir}(110)$  moiré is recognized with a wavelength of  $\lambda_m$  (typically  $\approx 3.3$  nm) distinctly larger than  $\lambda_{sm}$ .

The dark spots observed in the single-layer  $\text{MnBr}_2$  island of Figure 1(a) are attributed to

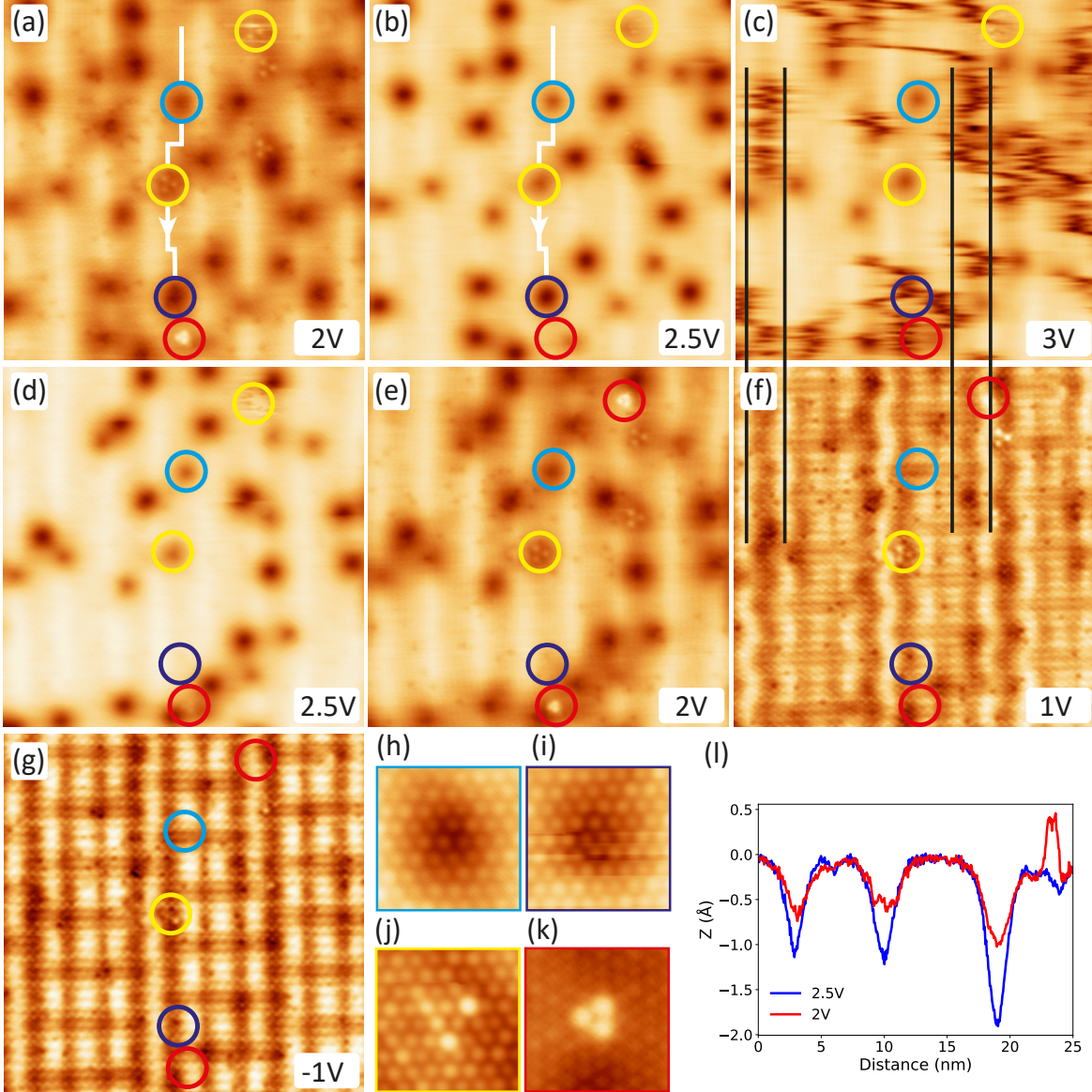


Figure 2. Polarons in single layer  $\text{MnBr}_2$ . (a)-(g) Successive STM topographs of the same sample location acquired at 4.2 K, with indicated  $V_b$  and  $I_t = 50$  pA. Polaron types are labeled as follows: light blue circle (type-I immobile), dark blue circle (type-I mobile), yellow circle (type-II  $2 \times 2$ ), and red circle (type-II  $1 \times 1$ ). Atomically resolved images of (h) type-I immobile, (i) type-I mobile, (j) type-II  $2 \times 2$ , and (k) type-II  $1 \times 1$  polarons. (l) Height profiles extracted along the white line in (a) and (b). Atomic resolution imaging parameters: (h,k)  $V_b = 2$  V and  $I_t = 1$  nA; (i)  $V_b = 1$  V and  $I_t = 1$  nA; (j)  $V_b = 2$  V and  $I_t = 100$  pA. Image sizes: (a)-(f)  $27$  nm  $\times$   $27$  nm; (g)-(j)  $2.7$  nm  $\times$   $2.7$  nm.

polarons in  $\text{MnBr}_2$ , as discussed below. The fuzzy stripe-like features arise from the mobility of the polarons driven by the interaction with the STM tip. The fuzzy polaron features partly align with the stripes of the super-moiré. This alignment indicates an interaction of

the polarons with the MnBr<sub>2</sub>/Gr/Ir(110) super-moiré.

To obtain more detailed insight, we imaged an MnBr<sub>2</sub> island area with high resolution while varying  $V_b$  between +3.0 V and -1 V, as presented in Figure 2. For positive  $V_b \geq 2$  V [Figure 2(a)-(e)] polarons and vertical bright stripes with  $\lambda_m = 3.3$  nm are present. For  $V_b \leq 1$  V [Figure 2(f)-(g)] the contrast of the polarons fades, the stripes with  $\lambda_m = 3.3$  nm disappear, and a new complex pattern consisting of vertical stripes with  $\lambda_{sm} = 2.7$  nm and horizontal stripe segments evolves. This pattern is the MnBr<sub>2</sub>/Gr/Ir(110) super-moiré [40]. We conclude that when tunneling is into the conduction band (conduction band edge is at 1.9 eV), only the corrugation of the Gr/Ir(110) moiré imprinted on the soft MnBr<sub>2</sub> layer modulates the tunneling current. However, with  $V_b < 1.9$  V electrons tunnel through the MnBr<sub>2</sub> band gap directly to the interface of MnBr<sub>2</sub> and Gr/Ir(110) from where the super-moiré originates [40].

Polarons imaged at  $V_b = +2.0$  V [Figure 2(a)] exhibit distinct shapes and heights. We distinguish four different types of polarons: type-I mobile polarons with the largest apparent depth of  $\approx 1$  Å (encircled dark blue), shallower type-I immobile polarons with a depth of  $\approx 0.7$  Å (encircled light blue), type-II  $2 \times 2$  polarons (encircled yellow), composed of three protrusions at the corners of a triangle with side length  $7.8$  Å (twice the MnBr<sub>2</sub> lattice parameter) within a shallow depression of about  $0.5$  Å, and type-II  $1 \times 1$  polarons (encircled red) composed of three bright protrusions of height  $\approx 0.5$  Å at the corners of a triangle of side length  $3.9$  Å (equal to the MnBr<sub>2</sub> lattice parameter). Atomically resolved images of the four types of polarons are shown in Figures 2(h)-(k). Although single-layer MnBr<sub>2</sub> exhibits occasional point defects, we did not observe a correlation between point defects and polaron positions or mobility. Depth and visibility of the polarons depends strongly on the sample bias applied as obvious from the voltage dependent series of Figure 2(a)-(g) and the comparison of the two height profiles for  $V_b = 2$  V and  $V_b = 2.5$  V in Figure 2(l) along the path indicated in Figures 2(a) and (b).

When imaging at  $V_b = +3.0$  V [Figure 2(c)], the fuzzy dark stripes appear that were already seen on large scale in Figure 1(b), indicating substantial mobility during scanning. Only a few polarons, visible as depressions remain in position. In fact, type-I mobile polarons are the most abundant species, making up 75% of all polarons. Upon lowering the sample bias back to  $V_b = 2.5$  V [Figure 2(d)], the mobile polarons become immobile again.

Applying again  $V_b = +2.0$  V [Figure 2(e)], identical to that in Figure 2(a), it is evident

that the type-I mobile polaron encircled dark blue in Figure 2(a) has changed position, as all other unmarked type-I mobile polarons. All other polarons remained stationary. Remarkably, a type-II  $2 \times 2$  polaron encircled yellow in Figure 2(a) has transformed into a type-II  $1 \times 1$  polaron encircled red in Figure 2(e).

Lowering the sample bias to  $V_b = +1.0$  V [Figure 2(f)] and even further to  $V_b = -1.0$  V [Figure 2(g)] reduces the visibility of individual polarons while at the same time the super-moiré of MnBr<sub>2</sub>/Gr/Ir(110) becomes prominent. In Figure 2(f), it can be recognized that the remaining type-II  $2 \times 2$  polarons are located at the minima of the super-moiré.

Some of the maxima of the super-moiré in Figure 2(e) marked by dashed black lines are extended to Figure 2(b). Although the fluctuations of the type-I mobile polarons occasionally extend in the horizontal direction over the black dashed lines, it is apparent that the fluctuations are predominantly confined between neighboring lines. The same feature has already been observed in Figure 1(b).

We therefore conclude that under the driving influence of the STM tip at sufficiently large positive sample bias, type-I mobile polarons experience a repulsive interaction with the maxima of the MnBr<sub>2</sub>/Gr/Ir(110) super-moiré. We note that type-I mobile polarons also move for large negative  $V_b$  as documented by a more extended data set shown as Figure S1 in the Supplementary Information (SI),

### **Charge State, Stability and Transformations of polarons**

A polaron is a localized charge dressed by lattice deformation. To substantiate our claim to observe polarons, we took constant height  $dI/dV$  point spectra on the four different polarons and a reference spectrum on a polaron-free area as shown in Figure 3(a). The spectra recorded on the different polarons exhibit an upward shift in the onset of the valence band, as expected for a localized negative charge. The spectrum of the type-I  $1 \times 1$  polaron displays an in-gap state at  $V_b \approx 1.2$  V. In the conduction band an upward shift in the onset appears as well, but the situation is less clear.

Therefore, we applied constant current  $dI/dV$  spectroscopy at the conduction band edge, which has proven to be extremely sensitive to detect band edges [42]. Lines of point spectra (briefly line spectra) shown in the lower panel of Figure 3(b) were taken along the paths as indicated by the arrows in the STM topographs of the upper panel of Figure 3(b). From

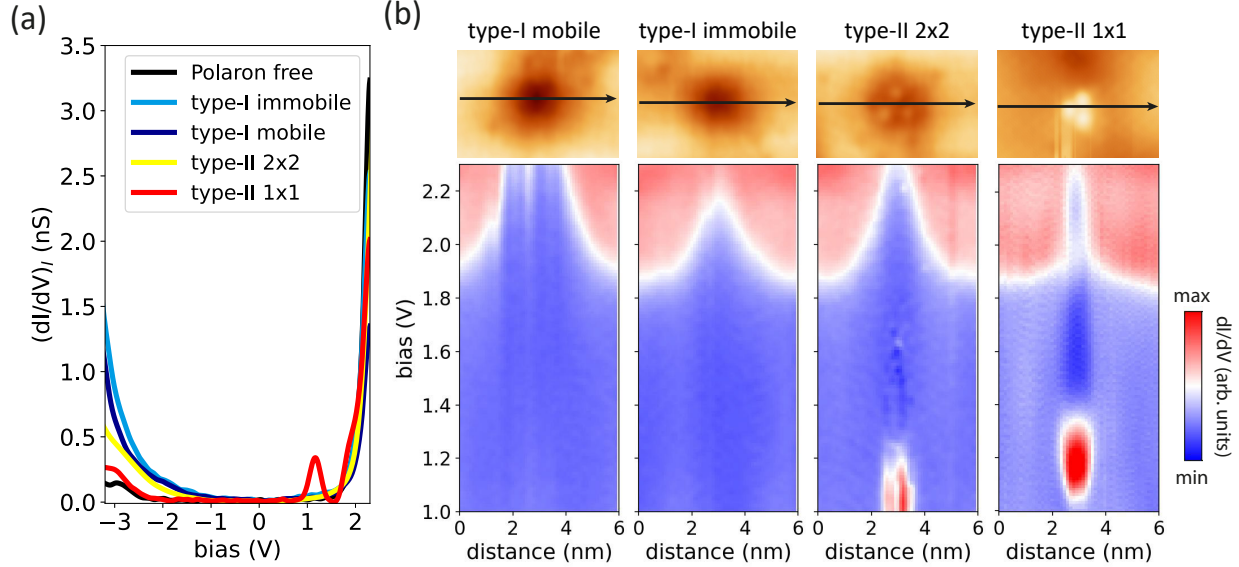


Figure 3. Band bending induced by polarons. (a) Constant height  $dI/dV$  point spectra taken on the polarons indicated compared to a reference spectrum without a polaron. (b) Lower panel: constant current  $dI/dV$  linescans over the type-I mobile, type-I immobile, type-II  $2 \times 2$ , and type-II  $1 \times 1$  polaron. Spectra are acquired with  $V_{st} = +2.3$  V,  $I_{st} = 50$  pA,  $f_{mod} = 667$  Hz, and  $V_{mod} = 20$  mV. Path of  $dI/dV$  linescans through polarons is indicated in STM topographs in the upper panels of the respective linescan maps. STM imaging parameters:  $V_b = 2$  V and  $I_t = 100$  pA and STM images size:  $6 \text{ nm} \times 4 \text{ nm}$ .

the line spectra, it is obvious that the polarons cause substantial upward band bending of the conduction band edge, as expected for the presence of a negative charge. The spatial extent of the band bending is of the order of  $\pm 2.5$  nm around the polaron center. The type-I  $1 \times 1$  polaron exhibits the strongest localization of band bending. Beyond the band bending, the type-II  $2 \times 2$  and type-II  $1 \times 1$  polarons exhibit in-gap states around 1 V and 1.2 V, respectively, attributable to localized polaronic states.

Polarons in  $\text{MnBr}_2$  on Gr/Ir(110) display a remarkable thermal stability. As shown in Figure 4(a) and (b) they are still present at 77 K and 300 K, respectively. Their number density decreases with temperature from  $\approx 0.06 \text{ nm}^{-2}$  at 4.2 K over  $\approx 0.04 \text{ nm}^{-2}$  at 77 K to  $\approx 0.01 \text{ nm}^{-2}$  at 300 K. However, the polaron number density at 300 K has presumably a large uncertainty, since at all  $V_b$  where polarons were visible, their interaction with the STM tip was noticeable.

The presence of polarons in single-layer  $\text{MnBr}_2$  on Gr/Ir(110) is independent of specific growth conditions. Up to now only polarons grown in samples at 450 K were presented. Figure 4(c) displays islands grown at  $\approx 80$  K, subject to unavoidable annealing to  $\approx 150$  K

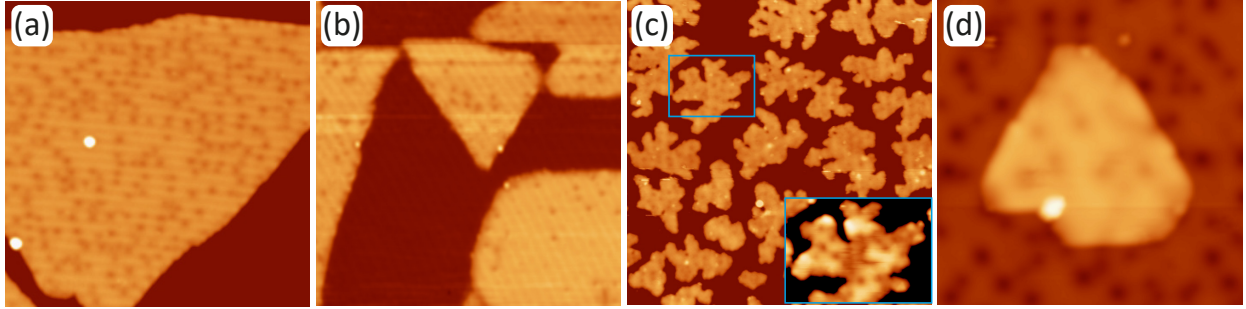


Figure 4. Thermal stability and growth independence of polarons in  $\text{MnBr}_2$  on  $\text{Gr/Ir(110)}$ . (a) Same sample as shown in Figure 1, but STM topograph acquired at 77 K. (b) STM topograph of a standard  $\text{MnBr}_2$  sample acquired at 300 K. (c) Sample after growth at  $\approx 80$  K and taken at 77 K with unavoidable annealing to  $\approx 150$  K in between due to sample transfer. The inset is a contrast-enhanced zoom of the area marked by a blue rectangle. (d) STM topograph with bilayer  $\text{MnBr}_2$  island. STM imaging parameters: (a-d)  $V_b = 2.5$  V,  $I_t = 20$  pA. Image sizes: (a-c)  $100$  nm  $\times$   $100$  nm and (d)  $35$  nm  $\times$   $35$  nm.

during UHV sample transfer to the STM, and imaged at 77 K. Even in the resulting fractal islands, polarons are present, as highlighted by the contrast-enhanced inset of Figure 4(c). Their concentration is comparable to that after  $\text{MnBr}_2$  growth at 450 K. Lastly, polarons are also visible in  $\text{MnBr}_2$  bilayers as shown in the STM topograph of Figure 4(d). However, it is not obvious whether these polarons are located in the first or the second  $\text{MnBr}_2$  layer. Whether polarons exist in thicker films could not be investigated due to increasing difficulties in imaging this insulator when its thickness increases.

The creation, annihilation, conversion and mobility of polarons was systematically investigated for the case of  $\text{CoCl}_2$  using a wide range of bias voltages with  $-3.5$  V  $\geq V_b \geq 4$  V and up to large tunneling currents  $I_t$  of 80 nA [22]. Here, a comparable analysis is hindered by the high polaron density and the fact that a voltage pulse simultaneously triggers multiple events in the ensemble. This is visualized in Figure 5(a) and (b), where a moderate voltage pulse causes not only the creation of a type-I mobile polaron, but also the motion of a nearby type-I mobile polaron to another position. Generally, type-II polarons easily convert into type-I mobile polarons [Figure 5(c-f)]. Type-II polarons also easily intraconvert, as shown for the conversion of a type-II  $1 \times 1$  into a type-II  $2 \times 2$  polaron in Figure 5(g) and (h). The opposite process, the conversion of a type-II  $2 \times 2$  polaron into a type-II  $1 \times 1$  polaron, was already observed in the sequence of Figure 2 and is symbolically indicated by the dashed arrow between Figure 5(g) and (h). We tentatively conclude that the type-I mobile polaron is energetically more favorable than the type-II polarons. A type-I immobile polaron could

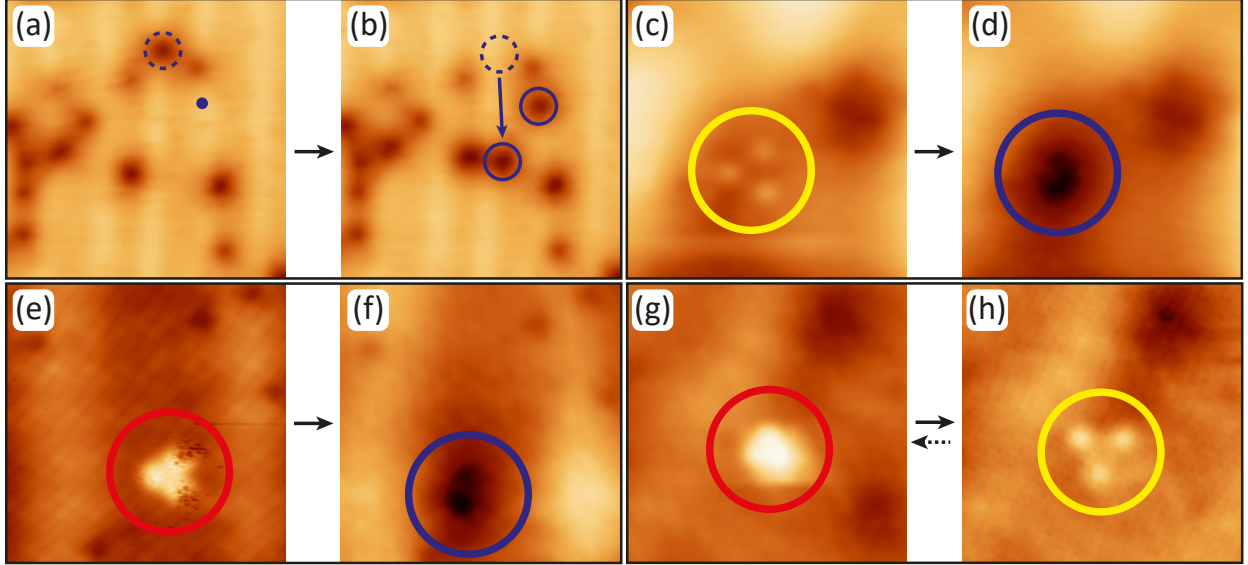


Figure 5. Polaron creation and conversion. (a) A voltage pulse with  $V_b = 3.5$  V and  $I_t = 5$  nA was set at the location indicated by the black dot. (b) The pulse created a type-I mobile polaron under the tip, but also caused a type-I mobile polaron to move (indicated by the arrow, original location encircled in dashed blue). (c) STM topograph of a type-II  $2 \times 2$  polaron. (d) STM topograph of the same area as in (c) after transformation of type-II  $2 \times 2$  polaron due to scanning into type-I mobile polaron. (e) STM topographs of type-II  $1 \times 1$  polaron. (f) STM topographs of the same area as in (e) after transformation of a type-II  $1 \times 1$  polaron into a type-II  $2 \times 2$  polaron during scanning. (g) STM topograph of type-II  $1 \times 1$  polaron. (h) STM topograph of the same area as in (g) after transformation of type-II  $1 \times 1$  polaron into a type-I mobile polaron during scanning. Scanning parameters: (a,b)  $V_b = 2.5$  V and  $I_t = 50$  pA, (c,d)  $V_b = 2$  V and  $I_t = 50$  pA, (e,f)  $V_b = 2$  V and  $I_t = 100$  pA, and (g,h)  $V_b = 1.5$  V and  $I_t = 100$  pA. Image sizes: (a,b)  $20$  nm  $\times$   $20$  nm and (c-h)  $6$  nm  $\times$   $6$  nm.

never be created or moved in the parameter space explored by us. This indicates that the type-I immobile polaron is either more stable than the other polarons or better screened against the tip electric field.

In Figure 2 motion of type-I mobile polarons was observed for  $V_b = 3$  V, but motion at lower positive  $V_b$  takes also place, when  $I_t$  is increased to maintain a low tunneling resistance [see Figure S2 of SI].

### Substrate Dependence of Polarons in $\text{MnBr}_2$

To clarify the influence of the substrate on the phenomenology of polarons, three single-layer  $\text{MnBr}_2$  samples were prepared on Gr/Ir(110), Gr/Ir(111) and Au(111). Gr on Ir(110) is structurally intact, but electronically the Dirac cone is absent due to substantial and

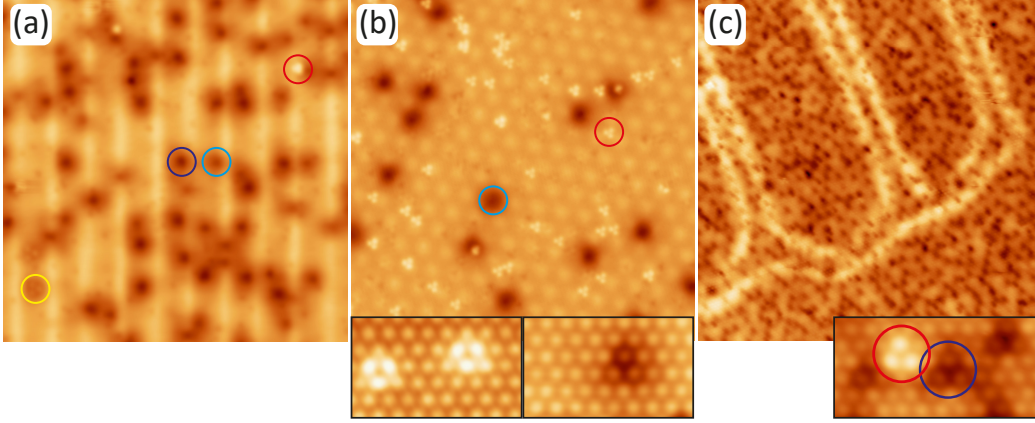


Figure 6. Comparison of polarons on different substrates: (a)  $\text{MnBr}_2/\text{Gr}/\text{Ir}(110)$ ; (b)  $\text{MnBr}_2/\text{Gr}/\text{Ir}(111)$ ; (c)  $\text{MnBr}_2/\text{Au}(111)$ . Polarons are encircled according to color code introduced in Figure 2 and used throughout. Insets (b) show high-resolution type-I immobile and type-II  $1 \times 1$  polaron. Inset (c) shows the type-I mobile and type II  $1 \times 1$  polaron in high resolution. STM imaging parameters: (a)  $V_b = 2 \text{ V}$ ,  $I_t = 50 \text{ pA}$ ; (b,c)  $V_b = 2.5 \text{ V}$ ,  $I_t = 20 \text{ pA}$ . Insets in (b)  $V_b = 1.5 \text{ V}$ ,  $I_t = 100 \text{ pA}$ , inset in (c)  $V_b = 2.5 \text{ V}$ ,  $I_t = 50 \text{ pA}$ . Image size in (a-c) is  $40 \text{ nm} \times 40 \text{ nm}$ , insets in (b)  $3.4 \text{ nm} \times 2 \text{ nm}$ , and inset in (c) is  $4 \text{ nm} \times 2 \text{ nm}$ .

inhomogeneous chemisorption. The Gr layer displays a  $sp^3$ -component in binding, making it slightly reactive to adsorption [43]. Gr on Ir(111) is physisorbed with an almost intact Dirac cone, marginal p-doping, and a clean  $sp^2$  character [44]. It can be considered an inert substrate, allowing the preparation of quasi-freestanding materials [45]. Although Au(111) is a noble metal surface, when used for the growth of transition metal chalcogenides, substantial band gap renormalization through hybridization and screening, reconstruction lifting, and the absence of charge density waves due to the interaction of the 2D material with the substrate were observed [46–48].

Using identical growth conditions, Figures 6(a)-(c) compare Gr/Ir(110), Gr/Ir(111) and Au(111) as substrates for single-layer  $\text{MnBr}_2$ , respectively. A comparison of larger scale topographs of the three samples is presented as Figure S3 in the SI. Already at first glance, Figure 6 makes clear that the differences in polaron phenomenology on the three different substrates are substantial. While  $\text{MnBr}_2$  on Gr/Ir(110) displays in Figure 6(a) four different types of polarons,  $\text{MnBr}_2$  on Gr/Ir(111) in Figure 6(b) and on Au(111) in Figure 6(c) exhibit only two types of polarons. The type-II  $1 \times 1$  polaron is present on all three substrates. On Gr/Ir(111) the type-I immobile polaron is additionally present, whereas the second polaron on Au(111) is tentatively assigned to be the type-I mobile polaron, as discussed in the

following.

Not only the number of polaron species detected, but also relative and total number densities of polarons differ on the three substrates. The total polaron number density on Au(111) is  $\approx 0.6$  polarons/nm<sup>-2</sup>, about an order of magnitude larger than for Gr/Ir(111) and Gr/Ir(110) with  $\approx 0.06$  polarons/nm<sup>-2</sup>. While on Gr/Ir(110) and Au(111) the type-I mobile polaron is by far the most abundant species, on Gr/Ir(111) it is the type-II  $1 \times 1$  polaron.

The apparent lateral extension of the type-I polarons in MnBr<sub>2</sub> differs also on the three different substrates. It is largest on Gr/Ir(111), slightly smaller on Gr/Ir(110) and considerably smaller on Au(111). One plausible explanation for these different sizes could be an increase of screening in going from Gr/Ir(111) (low density of states of Gr) to Au(111).

Although initially absent in MnBr<sub>2</sub> on Gr/Ir(111), the type-I mobile polaron can be easily created by conversion of a type-II  $1 \times 1$  polaron during scanning with  $V_b = 2.5$  V (see Supplementary Note 5 of the SI). In addition, creation of type-I mobile polarons with voltage pulses of  $V_b = 3.5$  V is straightforward (see Supplementary Note 6 of the SI). Due to the extremely high polaron density in MnBr<sub>2</sub> on Au(111) no statement can be made on polaron conversion or creation. Nevertheless, no other polaron species than the two already presented could be identified.

We note that the bright double lines in Figure 6(c) are dislocation lines of the Au(111) herringbone reconstruction. Their density is much lower than for pristine Au(111), which implies that due to MnBr<sub>2</sub> growth, the reconstruction was partially lifted.

Figure 7 provides additional insight into the differences in the electronic structure of MnBr<sub>2</sub> on the three different substrates by a comparison of  $dI/dV$  point spectra taken in areas without polarons.

MnBr<sub>2</sub> on Gr/Ir(110) and Gr/Ir(111) exhibits well defined band gaps with the valence band edge located at about -2.6 eV for both cases. However, for MnBr<sub>2</sub> on Gr/Ir(111) the band gap is clearly larger by about 0.4 eV with the edge of the conduction band located at 2.2 eV. For the case of MoS<sub>2</sub> a reduction in the size of the band gap (renormalization) due to the interaction with the substrate is well documented [46]. The smaller band gap size of MnBr<sub>2</sub> on Gr/Ir(110) compared to Gr/Ir(111) could therefore be attributed to a band gap renormalization caused by the stronger interaction of MnBr<sub>2</sub> with Gr/Ir(110).

For Au(111) as substrate, the measured  $dI/dV$  signal on MnBr<sub>2</sub> displays deviations from

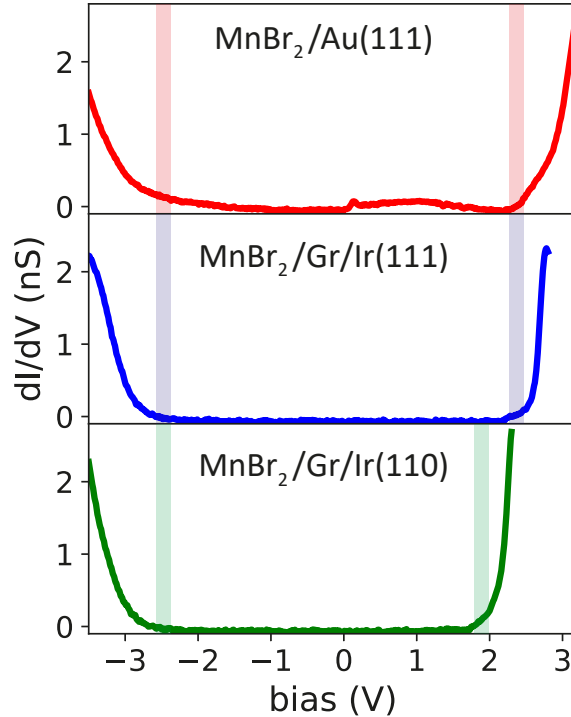


Figure 7. Comparison of constant height  $dI/dV$  point spectra of  $\text{MnBr}_2$  on different substrates. The conduction and valence band edges are marked by thick colored lines.  $dI/dV$  spectroscopy parameters:  $V_{st} = 3.5$  V for Au(111),  $V_{st} = +2.8$  V for Gr/Ir(111) and  $V_{st} = +2.3$  V [for Gr/Ir(110)],  $I_{st} = 50$  pA,  $f_{mod} = 667$  Hz, and  $V_{mod} = 20$  mV.

a plain band gap. First, a small step-like increase in the  $dI/dV$  level can be recognized at  $V_b = 0$  V, which remains until a steep rise at about  $V_b = 2.2$  V occurs. Second, the valence band edge appears to be less well defined with a gradual rise in the  $dI/dV$  intensity starting already at  $-1.5$  eV until it takes off at about  $V_b = -2.6$  V. We attribute these features to the local density of states of the metal surface underneath  $\text{MnBr}_2$ .

First, a step-like rise in  $dI/dV$  signal is known for the electron-like parabolic Au(111) surface state. However, the Au(111) surface state has its bottom at  $-0.5$  eV rather than at the Fermi level [49]. Upward shifts of the surface state by  $0.1$ - $0.3$  eV due to noble gas adsorption [49], growth of Gr [50], or growth of single-layer of  $\text{CoCl}_2$  [51] were reported. Since the surface state extends into the vacuum for pristine Au(111), one might speculate that polaron formation in the  $\text{MnBr}_2$  layer on Au(111) completely emptied the surface state, thereby moving its onset to the Fermi level.

Second, the density of states of Au is rather flat and dominated by an s-band in the vicinity of the Fermi level [52, 53]. It starts to increase at about  $-1.5$  eV below the Fermi

level towards lower energies through the d-band density of states. We speculate that it is this increase in the Au density of states, which by tunneling through  $\text{MnBr}_2$  – transparent in the band gap – is picked up with the STM.

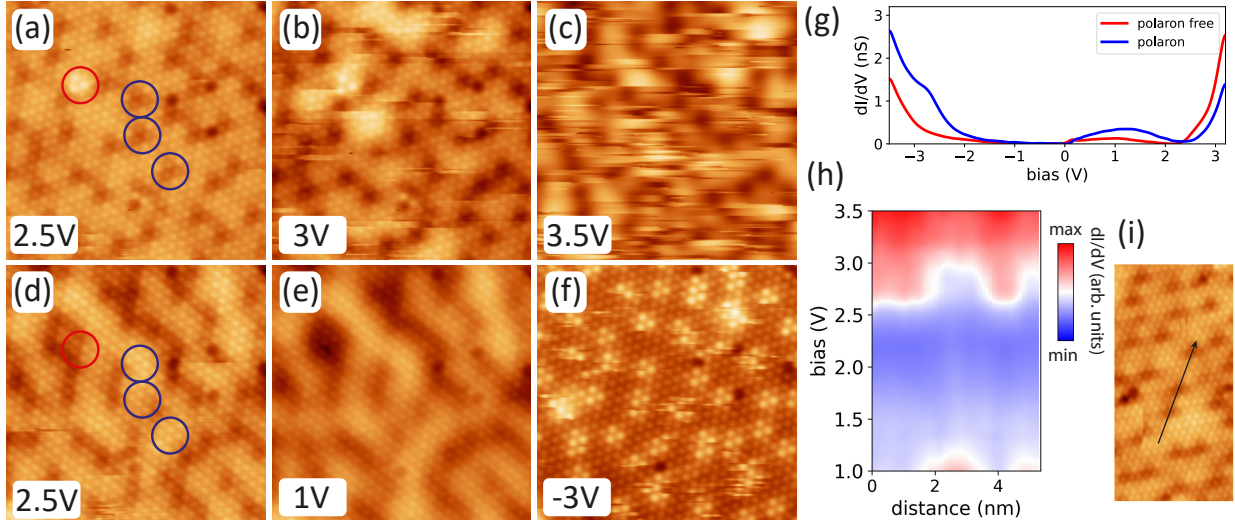


Figure 8. Sample bias dependence and electronic structure of polarons in single-layer  $\text{MnBr}_2$  on Au(111). (a-f) Sequence of high-resolution STM images of single-layer  $\text{MnBr}_2$  on Au(111) acquired at varying  $V_b$  as indicated and with  $I_t = 50$  pA. (g) Constant height  $dI/dV$  point spectrum on type-I mobile polaron compared to the reference spectrum from an area without polaron. (h) Constant current  $dI/dV$  line scan along the black arrow in the STM image shown in (i). STM imaging parameters: (i)  $V_b = +2.5$  V,  $I_t = 50$  pA. Constant height and constant current  $dI/dV$  spectroscopy parameters:  $V_{st} = +3.5$  V,  $I_{st} = 50$  pA,  $f_{mod} = 667$  Hz, and  $V_{mod} = 20$  mV. Image sizes: (a-f)  $10$  nm  $\times$   $10$  nm, (i)  $8$  nm  $\times$   $4$  nm.

The nature of the polarons in  $\text{MnBr}_2$  on Au(111) is further investigated by bias-dependent STM imaging as shown in Figure 8(a-f). In Figure 8(a) imaged at  $V_b = 2.5$  V a rare type-II  $1 \times 1$  polaron is encircled red, while three of the type-I mobile polarons are encircled blue. The latter form the overwhelming majority. Increasing the bias to  $V_b = 3$  V in Figure 8(b) shows first indications of polaron mobility. Fuzzy dark stripes appear in Figure 8(c) imaged with  $V_b = 3.5$  V. These fuzzy stripes are quite similar to those observed in  $\text{MnBr}_2$  on Gr/Ir(110) at  $V_b = 3$  V in Figure 2(c). The similar appearance and their mobility at large  $V_b$  justifies the assignment of these polarons as type-I mobile polarons. However, a difference from the situation on Gr/Ir(110) becomes obvious at negative  $V_b$ : after appearing as somewhat delocalized depressions in Figure 8(e) at  $V_b = 1$  V. at  $V_b = -3$  V as used in Figure 8(f), the polarons shine-up bright. Bright stripes at the polaron locations indicate some mobility also at  $V_b = -3$  V, again similar to polarons in  $\text{MnBr}_2$  to Gr/Ir(110) [compare Figure S1 of the

SI].

The constant height  $dI/dV$  spectrum of Figure 8(g) acquired on a polaron (blue), compared to a reference spectrum from the polaron-free area (red), reveals negative charge localized at the polaron site. This is obvious by the upward shift of both the valence and the conduction band edges as shown in Figure 8(g). The polaron spectrum displays near the valence band edge at about  $V_b = -2.8$  V an additional hump, which makes the polarons shine up bright in Figure 8(e) and is presumably a polaronic state. Additional intensity between the Fermi level at  $V_b = 0$  V and the conduction band edge is also observed at the polaron site. It could indicate a hybridization of the Au(111) surface state with a polaronic state. A constant current  $dI/dV$  line scan across polarons along the black arrow in Figure 8(h) along the path shown in Figure 8(i) confirms band bending due to negative charge at the polaron sites. It is also obvious from Figure 8(h) that the band bending is much more localized than for polarons on Gr/Ir(110), returning much faster to the base level of the conduction band edge. We interpret the more localized band bending as well as the more localized appearance of the polarons to be a consequence of enhanced screening by the metallic substrate.

For polarons in  $\text{MnBr}_2$  on Gr/Ir(111), information on voltage-dependent contrast, polaron induced band bending, polaron creation and mobility is found in Figures S4 to S6 of the SI.

## DISCUSSION

### *Comparison to polarons in single layers of other transition metal halides*

In recent years, polarons in single-layer transition metal halides were observed in several systems:  $\text{CoCl}_2$  [22, 23, 28, 29],  $\text{FeCl}_2$  (see Supporting Information of Ref. 22),  $\text{NiI}_2$  [25], and  $\text{CrBr}_3$  [26]. For all systems, polarons exhibit a similar global appearance (typically as a nano-sized depression). To focus the discussion, the results from single-layer  $\text{MnBr}_2$  are compared to single-layer  $\text{CoCl}_2$ , which, up to now, is the most thoroughly investigated among the transition metal halides [22, 23, 28, 29, 51].

Cai et al. [22] observed three different species of polarons in single-layer  $\text{CoCl}_2$  on highly oriented pyrolytic graphite (HOPG), Liu et al. [23] found two species on HOPG, Hao et al. [28] describe one species (which they consider as dipole solitons) on HOPG, and Kerschbaumer et al. [51] did not mention polarons on Au(111). However, polarons in  $\text{CoCl}_2$

seem to be present on Au(111) (see below).

Close similarity between the  $\text{MnBr}_2$  polaron properties and the most detailed observations of Cai et al. [22] is found. They describe three different species of polarons in  $\text{CoCl}_2$  named type-I (up), type-I (down), and type-II polaron. Due to their apparent similarity in their properties, they can be mapped onto the type-I mobile, type-I immobile, and type-II  $1 \times 1$  polarons in  $\text{MnBr}_2$ . In fact, the names of the  $\text{MnBr}_2$  polarons were chosen purposely to document the similarity to the polarons on  $\text{CoCl}_2$  and to avoid the introduction of unnecessary new terminology, but without imposing implications on the position of the charge, for which, in the case of  $\text{MnBr}_2$ , no sound evidence is present. Type-I polarons for both materials appear as depressions, with similar depth and size at  $V_b = 0.6 - 1.0$  V above the CBE. For both materials, the polarons tend to become invisible in the band gap. For both materials, the polarons with the deeper depression [type I mobile or (up)] can be easily moved with the STM tip. Lastly, for both materials, the type-I polarons display upward band bending of the CBE by about 0.5 eV. Given the similarity in appearance, bias-dependent changes, mobility, stability, and band bending, there can be little doubt that the type-I polarons in both materials are of a similar nature.

Cai et al. [22] also observe one species of the type-II polarons, which based on the data provided in ref. 22 can be mapped on the type-II  $1 \times 1$  polarons in  $\text{MnBr}_2$ . In both materials, the appearance of the polarons changes as a function of STM imaging voltage from a circular depression to a bright triangular protrusion within a circular shallow depression (compare Figure 2 and Supplementary Figure 6 of ref. 22). Upward bending of the CBE together with an in-gap polaronic state are observed.

Referring to the work of Liu et al. [23], their type-I and type-II polarons in single-layer  $\text{CoCl}_2$  on HOPG have to be mapped on the type-I (up) and type-I (down) polarons of Cai et al. [22], and thus correspond to type-I mobile and type-I immobile polarons in  $\text{MnBr}_2$ .

By STM Hao et al. and Song et al. [28, 29] also observed localized depressions in single-layer  $\text{CoCl}_2$  on HOPG which they interpret as localized dipoles (solitons). Based on similar phenomenology including their findings that solitons appear as depressions at positive sample bias and that some of them can be moved by the STM tip, we tentatively conclude that Hao et al. and Song et al. observe the same objects as described by Cai et al. and Liu et al. [22, 23], which correspond to the type-I polarons in  $\text{MnBr}_2$ .

For  $\text{MnBr}_2$ , we rule out the possibility that what we interpret as polarons are instead

localized charge dipoles. Figure 3 documents upward band bending at the polaron location caused by a negative charge. Due to the similar phenomenology in  $\text{MnBr}_2$  and  $\text{CoCl}_2$  our finding supports also for  $\text{CoCl}_2$  the polaron interpretation.

Kerschbaumer et al. [51] investigated the magnetism of single-layer  $\text{CoCl}_2$  on Au(111) and clearly observed polarons in high number density [compare Figure 1(a) of ref. 51], similar to what is found here for single-layer  $\text{MnBr}_2$  on Au(111). Even band bending and polaronic in-gap states are observed by STS (compare Figure 2 of ref. 51). Surprisingly, the possibility of polarons being present in single layers of  $\text{CoCl}_2$  on Au(111) is not mentioned in the manuscript. Also, Liu et al. imaged  $\text{CoCl}_2$  on Au(111) and the STM topographs of Fig. 19 presented in the Supplementary Information of ref. 23 display features similar to what is observed in  $\text{MnBr}_2$  on Au(111) and are interpreted by us as polarons.

Type-II  $2 \times 2$  polarons in  $\text{MnBr}_2$  cannot be mapped on any of the polarons experimentally described in transition metal dihalides so far. From the facile interconversion of type-II ( $2 \times 2$ ) and type-II ( $1 \times 1$ ) polarons [compare Figure 2(a) and (e) as well as Figure 5(g) and (h)] and their similar appearance as a triangular protrusion, it seems plausible that they are related and distinct from type-I polarons. We also note that theoretically only three different polarons were identified in transition metal halides [27], making the description of the fourth polaron species in transition metal halides a relevant finding.

### *Polaron stability*

Polarons in single-layer  $\text{MnBr}_2$  form spontaneously without external excitation. They are present in samples grown at 450 K and even in samples that never experienced a temperature above  $\approx 150$  K [see Figure 4(c)]. Their immediate presence in STM topographs at tunneling conditions for which no changes in polaron distribution or appearance occur is proof of this statement. Consequently, their presence is an equilibrium property and reduces the total energy of the system. This is not equivalent to a negative polaron formation energy  $E_{\text{pol}}$ , which is the energy gain of an electron when it transitions from a delocalized state at the bottom of the conduction band to a localized polaron. On a metal and in the absence of defects, one has to include the energy  $E_{\text{cbe}}$  needed to bring an electron from the Fermi level to the conduction band edge. Therefore, in thermodynamic equilibrium polarons are present if  $E_{\text{pol}} + E_{\text{cbe}} < 0$ . This implies for single-layer  $\text{MnBr}_2$  on Gr/Ir(110)  $E_{\text{pol}} < 1.9$  eV, since  $E_{\text{cbe}} \approx 1.9$  eV. The polaron formation energy  $E_{\text{pol}} = E_{\text{el}} + E_{\text{lat}}$  is composed of the electronic

energy gain  $E_{\text{el}}$  (negative) and the energy cost of the lattice distortion  $E_{\text{lat}}$  (positive) [3]. This implies  $E_{\text{el}} + E_{\text{cbe}} < 0$ , even in the limit of vanishing  $E_{\text{lat}}$ . As the lattice is frozen on the time scale of tunneling processes, in spectroscopy a polaronic state defined by  $E_{\text{el}} + E_{\text{cbe}}$  should be located below the Fermi level. If located above the Fermi level, the polaron could simply decay by tunneling of the trapped electron into an unoccupied metal state. We note that since  $\text{MnBr}_2$  has rather soft phonons,  $E_{\text{lat}}$  is presumably much smaller than the magnitude of  $E_{\text{el}}$ .

For type I-polarons in single-layer  $\text{MnBr}_2$  on Gr/Ir(110) STS detects no in-gap states, as obvious in Figure 3(a). The same holds for type-I polarons in  $\text{CoCl}_2$  [22, 23, 28]. In ref. 22 it was reasonably argued that the orbital character of the localized charge distribution may be inaccessible to STM which may hold for the present case as well. For type-I polarons on Au(111) it seems from Figure 8(g) that an in-gap state could be located about 3 eV below the Fermi level, consistent with Figure 8(f), where when imaging the sample with  $V_{\text{b}} = -3\text{ V}$  the polarons shine-up bright.

As obvious in Figure 3(b), for type-II polarons in-gap states are detected, but well above the Fermi level, again similar to  $\text{CoCl}_2$ , where such states were found in a similar distance below the conduction band edge. However, in the  $\text{CoCl}_2$  case, this placed them below the Fermi level. Why no in-gap states *below* the Fermi level are detected for type-II polarons in single-layer  $\text{MnBr}_2$  remains an open question.

The polaron formation energy  $E_{\text{pol}} < 1.9\text{ eV}$  estimated above is very large compared to other calculated polaron formation energies. DFT calculations for  $\text{CoCl}_2$  found  $E_{\text{pol}} \approx 0.2\text{ eV} - 0.3\text{ eV}$  [22, 23, 27], for instance. It is well known that defects may be a source of electrons, which are trapped in polaronic states [9, 10]. In single-layer  $\text{MnBr}_2$  grown on our substrates, we invariably find an appreciable concentration of point defects. In STM topographs, these are atomic sized dark spots, in which either no atom is visible or where the atom appears to sit a bit deeper, e.g., in Figure 2(f), Figure 8(f), Figure S2, and Figure S4-S6. One might speculate for instance that Br vacancies could provide electrons with a low ionization energy thereby acting as a source for electrons to be trapped in polarons. However, no correlation between defect location and polaron is observed. For example, Figures 2(h)-(k) do not show such defects, but only polarons. Point spectra at the defect locations show no band bending and no defect states close to the conduction band edge. Lastly, unlike a pure insulator, electrons liberated from defects in single-layer  $\text{MnBr}_2$  could tunnel into the substrate rather than

form a polaron, except if  $E_{\text{el}} + E_{\text{cbe}} < 0$ . This again would imply a very large magnitude of  $E_{\text{pol}}$ . In conclusion, based on the arguments provided – possibly incomplete – the estimated polaron formation energy for single-layer  $\text{MnBr}_2$  on a metallic substrate is surprisingly large.

*Consequences of substrate dependence of polarons in  $\text{MnBr}_2$*

It is remarkable that the three investigations of single-layer  $\text{CoCl}_2$  on HOPG [22, 23, 28] do not agree on the number of observed polaron (or soliton) species. This fact may indicate small differences in substrate preparation or growth procedure to be relevant. Our own experiments visualized in Figure 6 make plain that the substrate is indeed decisive for the number of species and the number density of polarons observed.

The immediate implication of these experimental findings is that an adequate modeling of polarons in single-layer transition metal dihalides is not possible without taking the substrate and its electronic properties into account. Thus, DFT calculations with a supercell containing only a single-layer cannot provide an adequate picture of the physical situation [22, 23, 27].

DFT calculations for rutile  $\text{TiO}_2$  interfacing  $\text{Cu}(100)$  by McKenna [54] showed that polaronic charge transfer from  $\text{Cu}$  to  $\text{TiO}_2$  leads to the formation of polarons in  $\text{TiO}_2$  next to the  $\text{Cu}/\text{TiO}_2$  interface. Polaronic charge transfer was found to lower the total system energy, with an initial energy gain of about 0.3 eV per polaron formed. A maximum of energy gain by polaron formation was found at a specific distance of the polarons from the interface which was saturated for a critical polaron number density. The interface dipole resulting from polaronic charge transfer introduces a band offset in  $\text{TiO}_2$  with an additional conduction band edge upshift that must be accounted for when considering vacuum level alignment between the two materials.

We speculate that DFT modeling similar to ref. 54 is needed taking the underlying metal into account to adequately describe polarons in single-layer transition metal halides. In any case, such a description for single-layer  $\text{MnBr}_2$  on a metallic substrate needs to explain the following features:

- (i) Polarons are spontaneously formed without external excitation. Their presence is an equilibrium property and does not depend on the details of the substrate.
- (ii) Polarons are present in a number density that depends on the substrate. Vacuum level alignment of metal and  $\text{MnBr}_2$  includes the interface dipole due to polaronic charge

transfer as a relevant factor, as also pointed out by McKenna [54]. The density of states of the substrate and the distribution of the charge at the metal surface are certainly of relevance in this respect. We take the shift of the Au(111) surface state in our  $dI/dV$  spectrum in Figure 7 as an indication that the large polaron density on Au(111) might be related to the localization of electrons that originate from the Au(111) surface state.

(iii) At least some of the polaron species present in a metal-insulator system are linked to their interface. Otherwise, the different numbers of polaron species present in  $\text{MnBr}_2$  on Gr/Ir(110) (four species), Gr/Ir(111) (two species) and Au(111) (two species) are not understandable. The omnipresence of the type-II  $1 \times 1$  polaron in all three systems may indicate that this polaron is not linked to the interface, while the type-II  $2 \times 2$  polaron being present only in  $\text{MnBr}_2$  on Gr/Ir(110) suggests that it is related to the complex interface of Gr/Ir(110) with  $\text{MnBr}_2$  [40]. The ease of inducing mobility and the ease of creation of the type-I mobile polaron by the STM tip suggest that the charge distribution of the type-I mobile polaron is closer to the surface rather than that of the type I immobile polaron, which might be located at the  $\text{MnBr}_2/\text{Gr}$  interface.

### *Polaron mobility*

If present or created by the STM tip, type-I mobile polarons in all three single layers  $\text{MnBr}_2$  systems become mobile at the sample biases above the conduction band edge, typically by 0.5 eV - 1 eV. The same behavior is observed for the corresponding polaron in  $\text{CoCl}_2$  [type-I (up)]. We interpret the onset of mobility to the population of the conduction band with electrons of sufficient energy and density able to excite phonons. Within this picture, mobility is primarily governed by phonon-assisted polaron hopping [1, 22], driven by inelastic electrons tunneling into the conduction band. The electric field at the polaron site, defined by the tip shape, sample bias, and tip-sample distance, can also be coupled to the trapped electron and the ionic displacement in  $\text{MnBr}_2$  and may exert a force when the tip is scanned across the polaron [22]. Its lateral component may be relevant for the direction of motion. However, we do not consider the field to be decisive for the onset of polaron mobility. In constant current STM mode, increasing the  $V_b$  from 2 V = 3 V leads to a tip retraction of approximately 3 Å due to the sharp rise in the accessible density of states once the conduction band is reached (see Figure S7 of the SI). This substantial increase in the tip-sample distance reduces the local electric field and therefore contracts, likely over-

compensating, the direct field enhancement expected from the higher bias, in precisely the bias range where type-I mobile polarons become mobile.

Although the limited spatial resolution at 300 K does not allow us to unambiguously assign the polaron species, the observation of stationary polarons at 300 K in MnBr<sub>2</sub> on Gr/Ir(110) [compare Figure 4(b)] provides an order of magnitude estimate of the hopping barrier. Describing the thermally activated motion of a polaron’s center of lattice deformation between nearest-neighbor sites by transition state theory,

$$\nu = \nu_0 e^{\frac{\Delta E}{k_B T}}$$

and adopting a standard prefactor  $\nu_0 = 5 \times 10^{12}$  consistent with the optical phonons frequency of  $\approx 150 \text{ cm}^{-1}$  of MnBr<sub>2</sub> [30], one obtains an activation barrier  $\Delta E = 0.87 \text{ eV}$  for an attempt frequency  $\nu \leq 10^{-2}$  consistent with the absence of mobility on the time scale of STM image acquisition.

For comparison, the highest calculated migration barriers reported for CoCl<sub>2</sub> polarons are 117 meV [22] and 100 meV [27], roughly a factor of eight smaller than the estimate above for MnBr<sub>2</sub> polarons. Given the phenomenological similarities between CoCl<sub>2</sub> and MnBr<sub>2</sub> polarons, this discrepancy is remarkable.

*Interaction of MnBr<sub>2</sub> polarons with the MnBr<sub>2</sub>/Gr/Ir(110) super-moiré*

A noteworthy observation in our experiments is the interaction of the type-I mobile polaron with the super-moiré of MnBr<sub>2</sub>/Gr/Ir(110). To our knowledge, an interaction of polarons in a transition-metal dihalide with a moiré has not been reported previously, even though this possibility has been checked [22, 23]. From Figure 1, Figure 2, and Figure S4, we conclude that the vertical stripe maxima of the MnBr<sub>2</sub>/Gr/Ir(110) super-moiré along the [1 $\bar{1}$ 0]-direction interact repulsively with type-I mobile polarons. The super-moiré constitutes a periodic electronic modulation arising from the interaction of the three involved materials, which may also involve structural distortions. While it appears most plausible that a periodic electrostatic potential associated with electronic modulation couples to trapped charge, it cannot be ruled out that periodic distortions of the super-moiré, if present, interact elastically with the deformation cloud of the polaron. Notably, polarons in single-layer CoCl<sub>2</sub> also appear to interact with the Au(111) herringbone reconstruction preserved under the layer.

Figure 1(a) of ref. 51 displays a clear correlation of polaron location and herringbone pattern. Taken together, these observations indicate that substrate-induced periodic potentials can measurably influence polaron energetics and spatial distributions, providing further evidence that adequate modeling of polarons in supported single-layer transition metal dichalcogenides must explicitly account for the substrate.

## CONCLUSIONS

Single-layers of  $\text{MnBr}_2$  on  $\text{Gr}/\text{Ir}(110)$  and  $\text{Gr}/\text{Ir}(111)$  host polarons of density  $\approx 6 \times 10^{-2}$  polarons/ $\text{nm}^{-2}$ , while on  $\text{Au}(111)$  the density is about an order of magnitude larger. Single-layer  $\text{MnBr}_2$  exhibits four types of polarons on  $\text{Gr}/\text{Ir}(110)$ , whereas changing the substrate to  $\text{Gr}/\text{Ir}(111)$  and  $\text{Au}(111)$ , only two types exist. All polarons exhibit upward band bending consistent with electron polarons. The lateral extent of the band bending is in the order of 5 nm on the  $\text{Gr}/\text{Ir}$  substrates but it is a factor of two smaller on  $\text{Au}(111)$ , presumably due to better screening.

On the  $\text{Gr}/\text{Ir}$  substrates, type-I mobile polarons can be created and interconverted with both type-II polarons by the STM tip. In contrast, no statements can be made in the  $\text{Au}(111)$  case due to the large polaron number density. Type-I mobile polarons move under the influence of a moving STM tip in tunneling contact, when electrons tunnel into states well above the conduction band edge, consistent with phonon-assisted mobility via inelastic tunneling. On  $\text{Gr}/\text{Ir}(110)$ , their motion is guided by the superperiodic potential of the super-moiré formed by  $\text{MnBr}_2$ ,  $\text{Gr}$ , and  $\text{Ir}(110)$ .

Of the four different species of polarons identified in  $\text{MnBr}_2$ , three closely resemble those in the paradigmatic  $\text{CoCl}_2$  on graphite system. This finding suggests that polarons are generic in transition metal halides and are of a similar nature across this material class. At least one polaron type is thermally stable and immobile up to 300 K, indicating a remarkably high barrier to thermal hopping. Since polarons are invariably present with reproducible number density and distribution of species when imaged gently, the polaron density measured at low temperatures reflects the frozen polaron distribution at some temperature below the growth temperature. The presence of an equilibrium distribution of polarons within tunneling distance to a conducting substrate implies a remarkably large magnitude of the polaron formation energy.

The interaction of polarons with the super-moiré patterns invites speculations. One could imagine that by patterning substrates, the possible pathways of motion and possible locations of polarons could be laterally predefined at the nanoscale. Together with their thermal stability at 300 K and the documented ability to create, move, and annihilate polarons this could open a door for information processing. However, thoughts in this direction are premature without a broader, more precise experimental determination of polaron properties in well-defined systems and their better understanding based on adequate modeling.

## EXPERIMENTAL SECTION

The samples were prepared in an ultrahigh vacuum chamber for molecular beam epitaxy with a base pressure below  $1 \times 10^{-10}$  mbar. Ir(110) is cleaned and prepared in its unreconstructed state using cycles of 1 keV Ar<sup>+</sup> sputtering, flash annealing to 1510 K, and subsequent cooling to 400 K in  $1 \times 10^{-7}$  mbar oxygen pressure. Ir(111) and Au(111) are cleaned through cycles of 1 keV Ar<sup>+</sup> ion sputtering and flash annealing to 1510 K for Ir(111) or 600 s annealing to 980 K for Au(111).

Single crystal Gr was grown by heating clean unreconstructed Ir(110) to 1510 K and then exposing it to  $3 \times 10^{-7}$  mbar ethylene for 240 s [43]. For Gr growth on Ir(111), the cleaned substrate was first exposed to  $1 \times 10^{-7}$  mbar ethylene at room temperature for 120 s and then flash annealed to 1470 K without ethylene. Subsequently, the sample is exposed for 600 s to  $3 \times 10^{-7}$  mbar ethylene at 1370 K, which completes the growth of a monolayer Gr [55].

MnBr<sub>2</sub> was grown at 450 K by sublimation of MnBr<sub>2</sub> molecules from MnBr<sub>2</sub> powder in a Knudsen cell heated to 670 K. The Knudsen cell was placed 8 cm from the sample, producing a deposition rate of  $3 \times 10^{-4}$  ML/s. Here, a monolayer (ML) corresponds to complete surface coverage by a single layer of MnBr<sub>2</sub>, equivalent to  $7.6 \times 10^{18}$  MnBr<sub>2</sub> molecules m<sup>-2</sup> s<sup>-1</sup>.

Once the preparation was completed, the sample was transferred under ultrahigh vacuum into the STM inside a bath cryostat that provides stable STM operation at 77 K and 4.2 K. Constant-current topographies were recorded with sample bias  $V_b$  and tunneling current  $I_t$ , as detailed in the respective figure captions. The STM images were analyzed and processed (plane subtraction, contrast correction) using WSxM software [56].  $dI/dV$  spectra were obtained at 4.2 K with stabilization bias  $V_{st}$  and stabilization current  $I_{st}$  using the standard

lock-in technique with modulation frequency  $f_{mod}$  and modulation voltage  $V_{mod}$ , as specified in the captions.

## ACKNOWLEDGMENTS

Funding from the Deutsche Forschungsgemeinschaft (DFG) through CRC 1238 (project number 277146847, subprojects A01, and B06) is acknowledged. J.F. acknowledges financial support from the DFG through project FI 2624/1-1 (project no. 462692705) within SPP 2137. W.J. acknowledges financial support by the DFG priority program SPP2244 (project no. 535290457). The authors acknowledge useful discussions with Tim Wehling, Achim Rosch, and Keith McKenna.

## CONFLICT OF INTEREST

The authors declare no conflict of interest.

## DATA AVAILABILITY STATEMENT

The data that support the findings of this study are available from the corresponding author upon reasonable request.

- 
- [1] C. Franchini, M. Reticcioli, M. Setvin, and U. Diebold, [Nat. Rev. Mater.](#) **6**, 560 (2021).
  - [2] A. J. E. Rettie, W. D. Chemelewski, D. Emin, and C. B. Mullins, [J. Phys. Chem. Lett](#) **7**, 471 (2016), pMID: 26758715.
  - [3] M. Reticcioli, U. Diebold, G. Kresse, and C. Franchini, Small polarons in transition metal oxides, in *Handbook of Materials Modeling: Applications: Current and Emerging Materials*, edited by W. Andreoni and S. Yip (Springer International Publishing, Cham, 2019) pp. 1–39.
  - [4] A. J. Tanner and G. Thornton, [J. Phys. Chem. Lett.](#) **13**, 559 (2022).
  - [5] C. Cheng, Z. Zhou, and R. Long, [J. Phys. Chem. Lett.](#) **14**, 10988 (2023).
  - [6] K. Miyata, D. Meggiolaro, M. T. Trinh, P. P. Joshi, E. Mosconi, S. C. Jones, F. D. Angelis, and X.-Y. Zhu, [Sci. Adv.](#) **3**, e1701217 (2017).

- [7] D. Ghosh, E. Welch, A. J. Neukirch, A. Zakhidov, and S. Tretiak, *J. Phys. Chem. Lett.* **11**, 3271 (2020).
- [8] T. Minato, Y. Sainoo, Y. Kim, H. S. Kato, K.-i. Aika, M. Kawai, J. Zhao, H. Petek, T. Huang, W. He, B. Wang, Z. Wang, Y. Zhao, J. Yang, and J. G. Hou, *J. Chem. Phys.* **130**, 124502 (2009).
- [9] M. Setvin, C. Franchini, X. Hao, M. Schmid, A. Janotti, M. Kaltak, C. G. Van de Walle, G. Kresse, and U. Diebold, *Phys. Rev. Lett.* **113**, 086402 (2014).
- [10] C. M. Yim, M. B. Watkins, M. J. Wolf, C. L. Pang, K. Hermansson, and G. Thornton, *Phys. Rev. Lett.* **117**, 116402 (2016).
- [11] M. Reticcioli, M. Setvin, X. Hao, P. Flauger, G. Kresse, M. Schmid, U. Diebold, and C. Franchini, *Phys. Rev. X* **7**, 031053 (2017).
- [12] M. Reticcioli, I. Sokolović, M. Schmid, U. Diebold, M. Setvin, and C. Franchini, *Phys. Rev. Lett.* **122**, 016805 (2019).
- [13] V. C. Birschtzky, I. Sokolović, M. Prezzi, K. Palotás, M. Setvín, U. Diebold, M. Reticcioli, and C. Franchini, *npj Comput. Mater.* **10**, 89 (2024).
- [14] C.-M. Yim, M. Allan, C. L. Pang, and G. Thornton, *J. Phys. Chem. C* **128**, 14100 (2024).
- [15] J. Redondo, M. Reticcioli, V. Gabriel, D. Wrana, F. Ellinger, M. Riva, G. Franceschi, E. Rheinfrank, I. Sokolović, Z. Jakub, F. Kraushofer, A. Alexander, E. Belas, L. L. Patera, J. Repp, M. Schmid, U. Diebold, G. S. Parkinson, C. Franchini, P. Kocan, and M. Setvin, *Sci. Adv.* **10**, eadp7833 (2024).
- [16] S. Sreekumar, P. Kocán, and M. Setvin, *Appl. Phys. Lett.* **127**, 140502 (2025).
- [17] C. Chen, J. Avila, S. Wang, Y. Wang, M. Mucha-Kruczyński, C. Shen, R. Yang, B. Nosarzewski, T. P. Devereaux, G. Zhang, and M. C. Asensio, *Nano Lett.* **18**, 1082 (2018).
- [18] M. Kang, S. W. Jung, W. J. Shin, Y. Sohn, S. H. Ryu, T. K. Kim, M. Hoesch, and K. S. Kim, *Nat. Mater.* **17**, 676 (2018).
- [19] P. Garcia-Goiricelaya, J. Lafuente-Bartolome, I. G. Gurtubay, and A. Eiguren, *Commun. Phys.* **2**, 81 (2019).
- [20] W. H. Sio and F. Giustino, *Nat. Phys.* **19**, 629 (2023).
- [21] C. van Efferen, L. Pätzold, T. Y. Tounsi, A. Schobert, M. Winter, Y. i. 't Veld, M. Georger, A. Safeer, C. Krämer, J. Fischer, J. Berges, T. Michely, R. Mozara, T. Wehling, and W. Jolie, *Phys. Rev. X* **15**, 031030 (2025).

- [22] M. Cai, M.-P. Miao, Y. Liang, Z. Jiang, Z.-Y. Liu, W.-H. Zhang, X. Liao, L.-F. Zhu, D. West, S. Zhang, and Y.-S. Fu, *Nat. Commun.* **14**, 3691 (2023).
- [23] H. Liu, A. Wang, P. Zhang, C. Ma, C. Chen, Z. Liu, Y. Zhang, B. Feng, P. Cheng, J. Zhao, L. Chen, and K. Wu, *Nat. Commun.* **14**, 3690 (2023).
- [24] Y. Liang, M. Cai, L. Peng, Z. Jiang, D. West, Y.-S. Fu, and S. Zhang, *J. Phys.: Condens. Matter* **37**, 145601 (2025).
- [25] M.-P. Miao, N. Liu, W.-H. Zhang, J.-W. Zhou, D.-B. Wang, C. Wang, W. Ji, and Y.-S. Fu, *PNAS* **122**, e2422868122 (2025).
- [26] M. Cai, Z. Jiang, W.-A. Liao, H.-J. Qin, W.-H. Zhang, J.-W. Zhou, L.-S. Liu, Y. Liang, D. West, S. Zhang, and Y.-S. Fu, *Nat. Commun.* **16**, 7117 (2025).
- [27] L. Yao, A. Wang, Q. Zheng, and J. Zhao, *Phys. Rev. B* **110**, 054305 (2024).
- [28] F. Hao, R. Song, J. Yang, J. Shen, A. Ernst, L. Yin, Z. Wang, and C. Gao, *Nano Lett.* **24**, 14042 (2024).
- [29] R. Song, F. Hao, J. Yang, L. Yin, and J. Shen, *Chin. Phys. B* **34**, 056802 (2025).
- [30] G. C. C. de Jesus, R. d. C. Vasconcelos, L. B. do Vale, R. F. de Menezes, K. G. Sprenger, and R. Gargano, *Langmuir* **41**, 5877 (2025).
- [31] J. Luo, G. Xiang, Y. Tang, K. Ou, and X. Chen, *J. Appl. Phys.* **128**, 113901 (2020).
- [32] V. V. Kulish and W. Huang, *J. Mater. Chem. C* **5**, 8734 (2017).
- [33] A. S. Botana and M. R. Norman, *Phys. Rev. Mater.* **3**, 044001 (2019).
- [34] X. Li, Z. Zhang, and H. Zhang, *Nanoscale Adv.* **2**, 495 (2020).
- [35] X. Bo, L. Fu, X. Wan, S. Li, and Y. Pu, *Phys. Rev. B* **109**, 014405 (2024).
- [36] E. O. Wollan, W. C. Koehler, and M. K. Wilkinson, *Phys. Rev.* **110**, 638 (1958).
- [37] Y. Farge, M. Régis, and B. Royce, *J. Phys.* **37**, 637 (1976).
- [38] K. Iio, H. Masuda, H. Tanaka, and K. Nagata, *J. Magn. Magn. Mater.* **90-91**, 265 (1990).
- [39] T. Sato, K. Iio, H. Kadowaki, and H. Masuda, *J. Phys. Soc. Jpn.* **63**, 4583 (1994).
- [40] A. Safeer, O. Güleriyüz, N. Atodiresei, W. Jolie, T. Michely, and J. Fischer, *MnBr<sub>2</sub> on the graphene on Ir(110) substrate: growth, structure, and super-moiré* (2025), arXiv:2508.19694 [cond-mat.mtrl-sci].
- [41] C. Ronda, H. Siekman, and C. Haas, *Physica B+C* **144**, 331 (1987).
- [42] C. Murray, W. Jolie, J. A. Fischer, J. Hall, C. van Efferen, N. Ehlen, A. Grüneis, C. Busse, and T. Michely, *Phys. Rev. B* **99**, 115434 (2019).

- [43] S. Kraus, F. Huttmann, J. Fischer, T. Knispel, K. Bischof, A. Herman, M. Bianchi, R.-M. Stan, A. J. Holt, V. Caciuc, S. Tsukamoto, H. Wende, P. Hofmann, N. Atodiresei, and T. Michely, [Phys. Rev. B \*\*105\*\*, 165405 \(2022\)](#).
- [44] C. Busse, P. Lazić, R. Djemour, J. Coraux, T. Gerber, N. Atodiresei, V. Caciuc, R. Brako, A. T. N'Diaye, S. Blügel, J. Zegenhagen, and T. Michely, [Phys. Rev. Lett. \*\*107\*\*, 036101 \(2011\)](#).
- [45] J. Hall, B. Pielić, C. Murray, W. Jolie, T. Wekking, C. Busse, M. Kralj, and T. Michely, [2D Mater. \*\*5\*\*, 025005 \(2018\)](#).
- [46] A. Bruix, J. A. Miwa, N. Hauptmann, D. Wegner, S. Ulstrup, S. S. Grønborg, C. E. Sanders, M. Dendzik, A. Grubišić Čabo, M. Bianchi, J. V. Lauritsen, A. A. Khajetoorians, B. Hammer, and P. Hofmann, [Phys. Rev. B \*\*93\*\*, 165422 \(2016\)](#).
- [47] C. E. Sanders, M. Dendzik, A. S. Ngankeu, A. Eich, A. Bruix, M. Bianchi, J. A. Miwa, B. Hammer, A. A. Khajetoorians, and P. Hofmann, [Phys. Rev. B \*\*94\*\*, 081404 \(2016\)](#).
- [48] R.-M. Stan, S. K. Mahatha, M. Bianchi, C. E. Sanders, D. Curcio, P. Hofmann, and J. A. Miwa, [Phys. Rev. Mater. \*\*3\*\*, 044003 \(2019\)](#).
- [49] T. Andreev, I. Barke, and H. Hövel, [Phys. Rev. B \*\*70\*\*, 205426 \(2004\)](#).
- [50] P. Leicht, L. Zielke, S. Bouvron, R. Moroni, E. Voloshina, L. Hammerschmidt, Y. S. Dedkov, and M. Fonin, [ACS Nano \*\*8\*\*, 3735 \(2014\)](#).
- [51] S. Kerschbaumer, S. E. Hadjadj, A. Aguirre-Baños, D. Longo, A. Pinar Solé, O. Stetsovych, A. E. Candia, P. Angulo-Portugal, D. Caldevilla, F. Choueikani, M. Corso, D. Serrate, J. Lobo-Checa, P. Jelínek, M. Ilyn, and C. Rogero, [ACS Nano \*\*19\*\*, 20693 \(2025\)](#).
- [52] N. V. Smith, [Phys. Rev. B \*\*9\*\*, 1365 \(1974\)](#).
- [53] P. Norton, R. Tapping, and J. Goodale, [Surf. Sci. \*\*72\*\*, 33 \(1978\)](#).
- [54] K. P. McKenna, [Phys. Rev. B \*\*94\*\*, 155147 \(2016\)](#).
- [55] J. Coraux, A. T N'Diaye, M. Engler, C. Busse, D. Wall, N. Buckanie, F.-J. Meyer zu Heringdorf, R. van Gastel, B. Poelsema, and T. Michely, [New J. Phys. \*\*11\*\*, 023006 \(2009\)](#).
- [56] I. Horcas, R. Fernández, J. M. Gómez-Rodríguez, J. Colchero, J. Gómez-Herrero, and A. M. Baro, [Rev. Sci. Instrum. \*\*78\*\*, 013705 \(2007\)](#).

## SUPPLEMENTARY INFORMATION

Supplementary note 1: Extended dataset for bias-dependent polaron imaging and mobility.

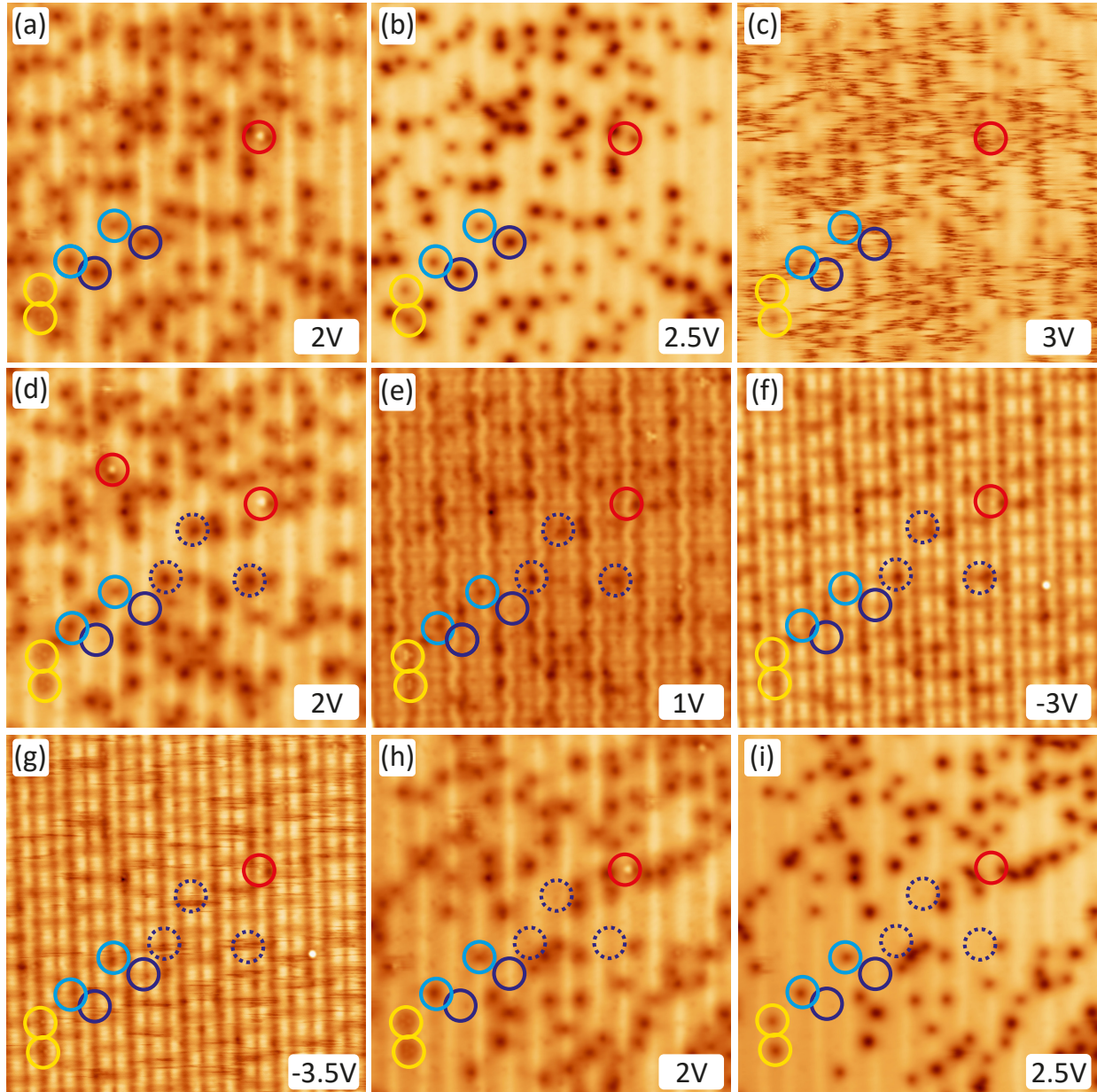


Figure 1. (a-i) Sequence of STM images of the same area acquired at varying  $V_b$  ranging from +3 V and  $-3.5$  V, as indicated, and at  $I_t = 50$  pA. Selected polarons are encircled to track their position: dark blue (type-I mobile), light blue (type-I immobile), yellow (type-II 2x2), and red (type-II 1x1). From comparison of (d) and (h) it is obvious that type-I mobile polarons are also moved at  $V_b = -3.5$  V. Image sizes:  $45$  nm  $\times$   $45$  nm.

Figure 1 presents a complementary dataset to Figure 2 of the main text, extending the investigation to higher negative bias range. The behavior at positive  $V_b$  [Figure 1(a-e)] is consistent with our previous observations. The four types of polarons are distinguishable at  $V_b = 2\text{ V}$ , and type-I mobile polarons change positions after increasing  $V_b$  to  $3\text{ V}$ , as tracked by the polarons encircled dark blue in Figure 1(a-d).

The tip-induced mobility is also observed at negative  $V_b$ . If  $V_b$  is set to  $-3.5\text{ V}$  in Figure S1(g), type-I mobile polarons are mobile as obvious from the comparison of Figures S1(d) and (h) (check position in dotted dark blue circles).

**Supplementary note 2: Mobility of type-I mobile polaron for lower positive  $V_b$  at large tunneling current**

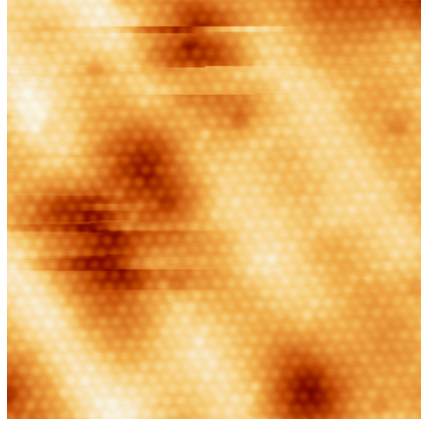


Figure 2. STM image acquired with  $V_b = 2\text{ V}$ ,  $I_t = 3\text{ nA}$ . Image size:  $15\text{ nm} \times 15\text{ nm}$ .

**Supplementary Note 3: Overview topographs of single-layer  $\text{MnBr}_2$  grown on different substrates.**

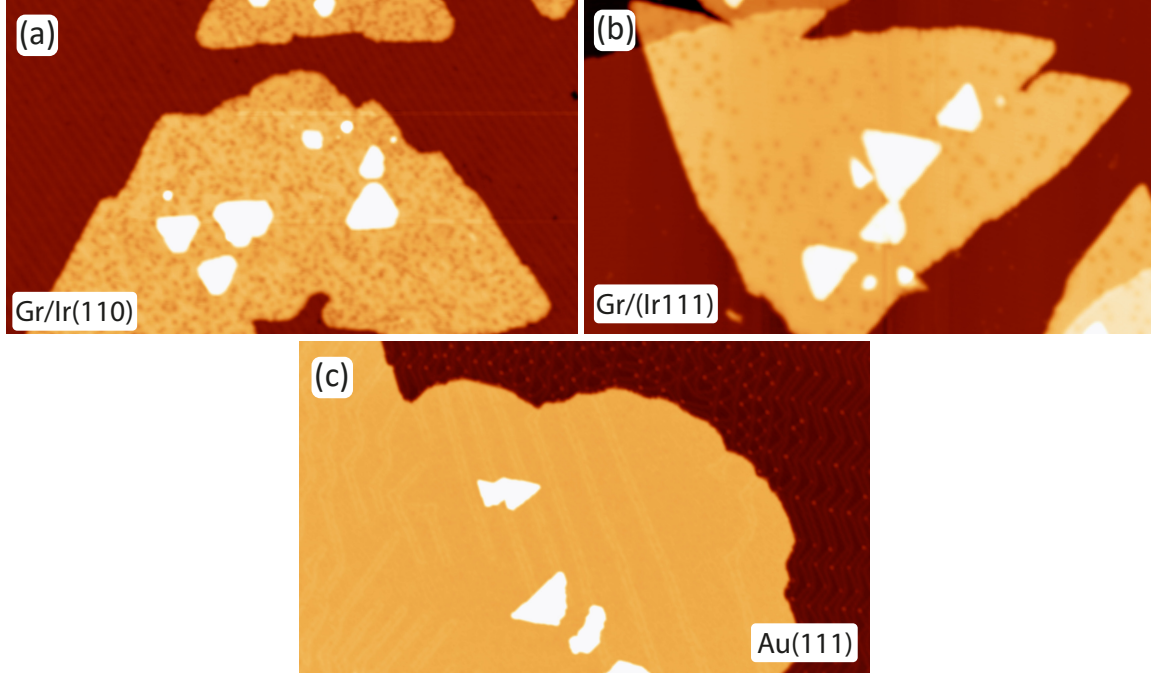


Figure 3. (a) Overview STM topographs of  $\text{MnBr}_2$  on (a) Gr/Ir(110), (b) Gr/Ir(111) and (c) Au (111). STM Imaging Parameters: (a)  $V_b = 3.5 \text{ V}$ ,  $I_t = 20 \text{ pA}$ , (b)  $V_b = 3.5 \text{ V}$ ,  $I_t = 20 \text{ pA}$ , (c)  $V_b = 2 \text{ V}$ ,  $I_t = 50 \text{ pA}$ . Image sizes:  $240 \text{ nm} \times 140 \text{ nm}$ .

On top of single-layer  $\text{MnBr}_2$  islands also small second-layer  $\text{MnBr}_2$  islands are visible. The overview STM image of  $\text{MnBr}_2$  on Au(111) in Figure S3 shows the herringbone reconstruction in the island, which is only partly lifted by  $\text{MnBr}_2$  overgrowth.

#### Supplementary note 4: Polarons in $\text{MnBr}_2$ on $\text{Gr}/\text{Ir}(111)$

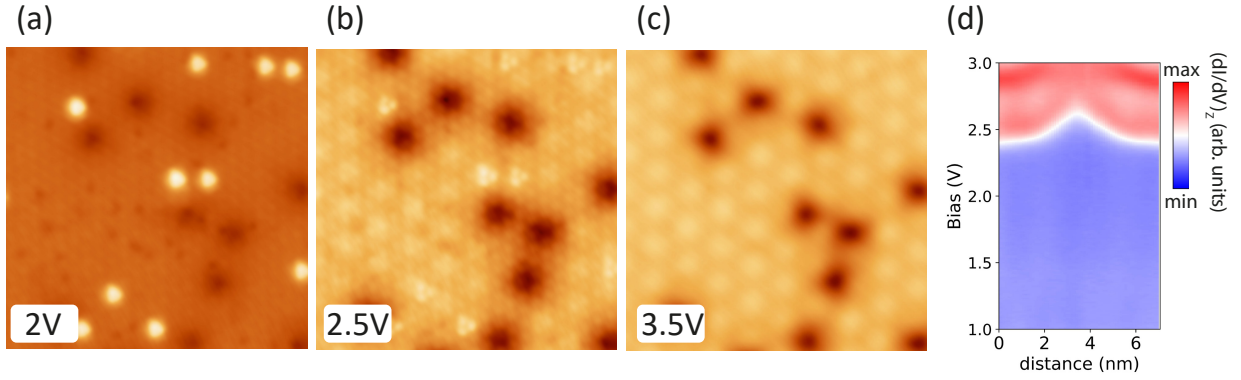


Figure 4. (a-c) Consecutive STM topographs of  $\text{MnBr}_2$  on  $\text{Gr}/\text{Ir}(111)$  at different  $V_b$  as indicated. (d) Constant current  $dI/dV$  linescan map over the type-I immobile, Spectra are acquired with  $V_{st} = +3$  V,  $I_{st} = 50$  pA,  $f_{mod} = 667$  Hz, and  $V_{mod} = 20$  mV. STM imaging parameters:  $I_t = 50$  pA. Image sizes:  $18 \text{ nm} \times 18 \text{ nm}$ .

**Supplementary note 5: Tip induced conversions of type-II 1x1 polarons into type-I mobile polarons.**

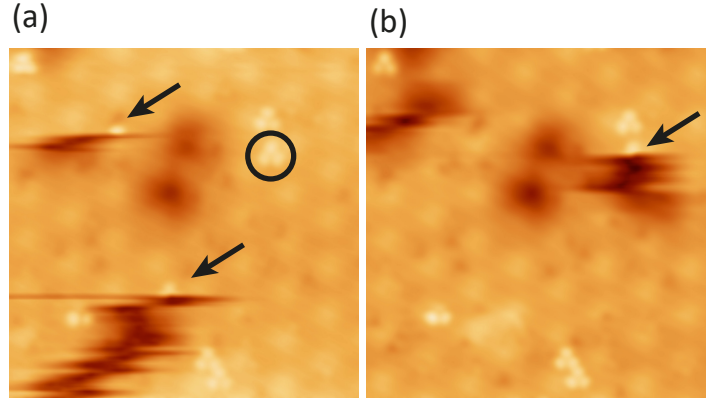


Figure 5. (a,b) Consecutive STM topographs of  $\text{MnBr}_2$  on  $\text{Gr}/\text{Ir}(111)$ . The black arrows in (a) indicate locations where the STM tip induces a conversion from a type-II 1x1 polaron to type-I mobile polaron. Additionally, also the type-II 1x1 polaron circled in (a) has converted to a type I mobile polaron in (b), as highlighted by the arrow in (b). STM imaging parameters:  $V_b = 2.5 \text{ V}$ ,  $I_t = 50 \text{ pA}$ . Image sizes:  $18 \text{ nm} \times 18 \text{ nm}$ .

Figure 5 demonstrates conversions of type-II 1x1 polarons to type-I mobile polarons induced during STM scanning. After these conversions, the type-I mobile polarons move with the tip, appearing as fuzzy and continuous dark features in the topographs.

**Supplementary note 6: Creation of a type-I 1x1 mobile polaron in MnBr<sub>2</sub> on Gr/Ir(111).**

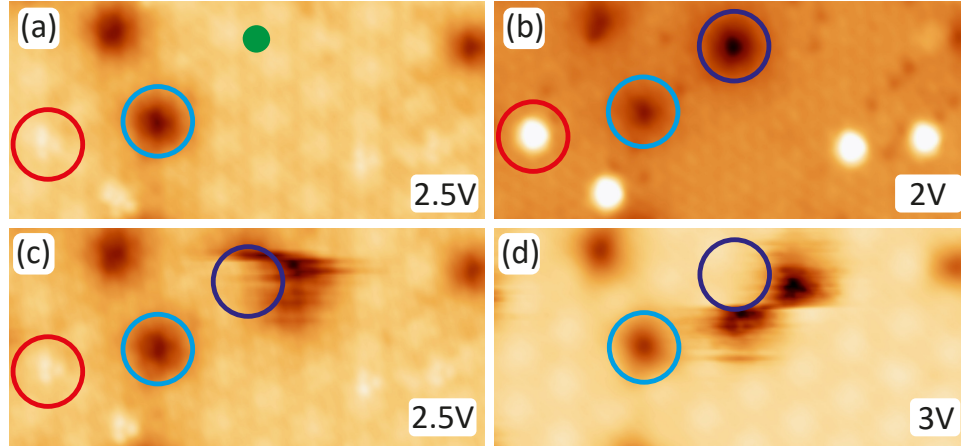


Figure 6. Sequence of STM images illustrating the creation of a type-I mobile polaron in MnBr<sub>2</sub> on Gr/Ir(111) via bias pulsing. (a) STM topograph before bias pulsing with pre-existing type-II 1x1 and type-I immobile polarons (circled red and light blue, respectively). (b) STM topograph after bias pulse with  $V_b = +3.5$  V and  $I_t = 500$  pA at green dot in (a). (c,d) Subsequent imaging at higher biases shows the mobile polaron moving under the influence of the STM tip.  $I_t = 50$  pA. Image sizes: 22 nm  $\times$  10 nm.

Figure 6 shows the creation of a type-I mobile polaron. A bias pulse ( $V_b = +3.5$  V,  $I_t = 500$  pA) is applied at the green spot in Figure 6 (a). Subsequent imaging at  $V_b = +2$  V, as shown in Figure 6(b), reveals a type-I mobile polaron (encircled purple) at pulse location along with pre-existing type-I immobile (encircled blue) and type-II 1x1 polarons (encircled red). In subsequent imaging at  $V_b = +2.5$  V and +3 V in Figure 6(c) and (d) the observed mobility of the polaron justifies its classification as type-I mobile polaron.

Supplementary note 7: Bias dependent absolute tip heights above Gr/Ir(110) and MnBr<sub>2</sub>/Gr/Ir(110).

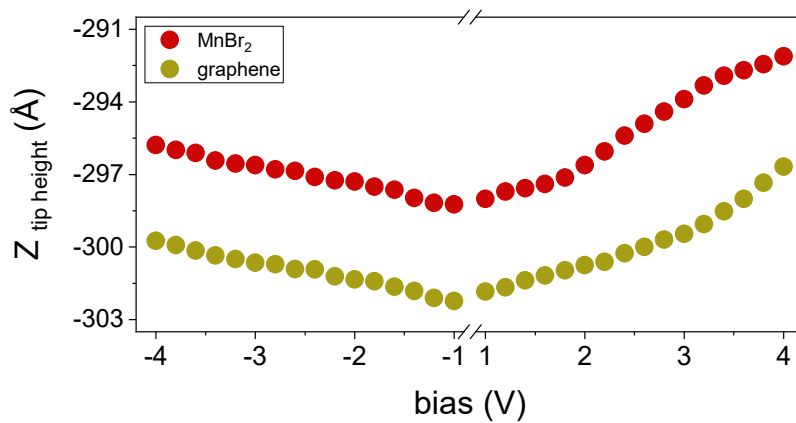


Figure 7. Absolute heights of the STM tip over Gr/Ir(110) (red squares, right  $y$ -axis) and MnBr<sub>2</sub>/Gr/Ir(110) (black squares, left  $y$ -axis) for  $I_t = 20$  pA as a function of  $V_b$ .